Mechanics of Precurved-Tube Continuum Robots

Robert J. Webster, III, *Member, IEEE*, Joseph M. Romano, *Student Member, IEEE*, and Noah J. Cowan, *Member, IEEE*

***Abstract*—This paper presents a new class of thin, dexterous continuum robots, which we call active cannulas due to their potential medical applications. An active cannula is composed of telescoping, concentric, precurved superelastic tubes that can be axially translated and rotated at the base relative to one another. Active cannulas derive bending not from tendon wires or other external mechanisms but from elastic tube interaction in the backbone itself, permitting high dexterity and small size, and dexterity improves with miniaturization. They are designed to traverse narrow and winding environments without relying on "guiding" environmental reaction forces. These features seem ideal for a variety of applications where a very thin robot with tentacle-like dexterity is needed. In this paper, we apply beam mechanics to obtain a kinematic model of active cannula shape and describe design tools that result from the modeling process. After deriving general equations, we apply them to a simple three-link active cannula. Experimental results illustrate the importance of including torsional effects and the ability of our model to predict energy bifurcation and active cannula shape.**

***Index Terms*—Continuum robot, flexible manipulator, medical robot, snake-like robot.**

I. Introduction and Background

ROBOTIC dexterity at the "meso scale"—from hundreds of micrometers to tens of centimeters—remains a challenge. Construction of traditional actuated serial-link chains at this scale requires intricate fabrication, integration, and instrumentation. Continuously flexible ("continuum") robots [1]–[6] provide an alternative, although most designs require wires [5], [7], [8], flexible push rods [9], pneumatic actuators [4], [6], or other external actuation mechanisms that limit miniaturization.

Here, we describe a new class of miniature continuum robots, which we call active cannulas, that have the potential to bridge this gap and impact a wide range of applications in confined, tortuous environments. For example, in interventional medicine, such devices may provide minimally invasive access to challenging or currently unreachable surgical sites.

Manuscript received January 11, 2008; revised June 28, 2008. First published November 11, 2008; current version published February 4, 2009. This paper was recommended for publication by Associate Editor C. Cavusoglu and Editor H. Arai upon evaluation of the reviewers' comments. This paper was presented in part at the IEEE/RSJ International Conference on Intelligent Robots and Systems (IROS), 2006, and the IEEE International Conference on Robotics and Automation (ICRA), 2008. Relevant portions are patent pending. This work was supported by the National Science Foundation under Grant 0651803.

R. J. Webster is with Vanderbilt University, Nashville, TN 37235 USA (e-mail: robert.webster@vanderbilt.edu).

J. M. Romano is with the University of Pennsylvania, Philadelphia, PA 19104 USA.

N. J. Cowan is with Johns Hopkins University, Baltimore, MD 21218 USA (e-mail: ncowan@jhu.edu).

Color versions of one or more of the figures in this paper are available online at http://ieeexplore.ieee.org.

Digital Object Identifier 10.1109/TRO.2008.2006868

Minimally invasive surgery (MIS) has profoundly changed interventional medicine in recent years, reducing trauma and speeding healing. However, many possible intervention sites lack viable minimally invasive alternatives because current rigid (and generally straight) instruments cannot reach them. These sites may require navigating entry pathways that are narrow or contain complex 3-D bends. Accessing them requires the surgical tool to "turn corners" and maintain dexterity after doing so. These constraints render confined surgical sites off limits to current commercial surgical robots, as well as manual MIS tools. Standard clinical designs for both are characterized by relatively large diameters (typically 5–10 mm), rigid shafts, and (in the case of manual tools) lack of end-effector dexterity. While optimal port placement seeks to allow reasonable workspace volume with port constraints [10], [11], there is little flexibility in port placement when accessing surgical sites through natural orifices (e.g., throat or nostrils), which often offer the least invasive entry paths. This motivates a move away from straight rigid tools toward actively shapable flexible instruments like active cannulas.

Active cannulas are MIS devices that can be thinner or more dexterous than existing medical continuum robots, laparoscopic robots, or manual laparoscopic tools. They are a new class of miniature continuum robots that derive bending actuation not from tendon wires or other external mechanisms, but from elastic interaction of curved tubes that form the "backbone" of the device. This makes them sufficiently flexible and shapable to traverse bends and corners to access confined anatomical locations.

A number of clinical applications may substantially benefit from active cannulas, and similar designs have been proposed for fetal surgery [12], steering needles in soft tissues [13], [14] and cardiac applications [14], transnasal skull base and transgastric surgery [15]–[17], and minimally invasive access deep within the lung [18]. Several specific clinical areas in which active cannulas could improve surgical outcomes are described in detail in [19].

A. Related Work

Active cannulas are composed of precurved superelastic component tubes that can extend telescopically and rotate axially with respect to one another (Fig. 1). Beam-mechanics-based models accounting for the effects of both translation and rotation of telescoping, concentric elastic tubes were first presented by our group [15], [18], and Sears and Dupont [14]. Developed concurrently and independently, these models are strikingly similar: under similar assumptions, both describe the equilibrium conformations of concentric precurved elastic tubes as a function of base angles of rotation. One difference between the two studies is torsion, which is assumed negligible in [14] but is included in transmission (the straight segments beginning at the

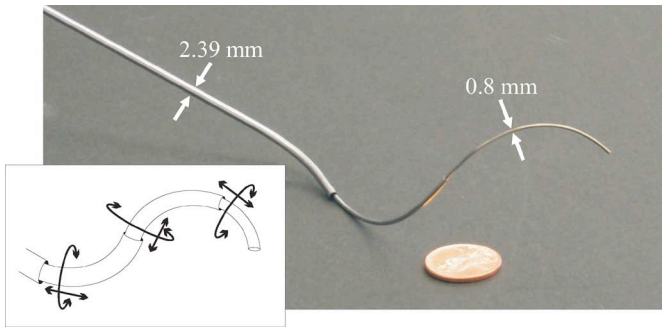

Fig. 1. Prototype active cannula made of superelastic Nitinol tubes. The inset line drawing indicates the active cannula's degrees of freedom.

actuators and ending at the start of precurvature) in [15]. Without torsional compliance, the kinematics of an active cannula can be expressed in closed form. Including torsion in transmission leads to transcendental equations that must be solved numerically. While a framework for multilink forward and inverse kinematics without torsion has been formulated [20], it has not yet been experimentally validated. Thus, our objectives in the following sections are to derive a multilink kinematic framework that includes torsion, determine model parameters via calibration, and experimentally assess the accuracy and descriptive capability of models with and without torsion.

Our research builds on several other recently published designs. Loser developed a steerable needle composed of two fully overlapping precurved cannulas that could be rotated (but not translated) with respect to one another to change needle curvature [13]. Another design with some similarity to active cannulas was proposed by Furusho *et al.*, who describe a "curved multitube" (CMT) also with two curved cannulas that rotate but do not translate, through which a needle is deployed [12], [21], as well as a conceptual design sketch of a device similar to the steerable needle of [22] described shortly. CMT modeling has thus far assumed infinite flexural rigidity of each outer tube compared to all those inside it, as well as infinite torsional rigidity, and we relax both of these assumptions. Similarly, Okazawa *et al.* describe a steerable needle with a stiff outer cannula and a single flexible curved interior wire that can extend and rotate to control steering magnitude and direction as the needle is pushed into tissue [22], and Daum patented a deflectable needle assembly that deploys a curved "catheter" through a rigid outer cannula [23].

While the location of actuation (at the base, outside the body) is similar to both catheters and steerable needles [24]–[27], active cannulas employ a fundamentally different means of steering than either. Specifically, catheters use blood vessel reaction forces to direct them down desired branches, and needles rely on reaction forces from surrounding tissue to steer; in contrast, active cannulas require no tissue reaction forces, deriving steering from internal moments that tubes apply on each other.

B. Contributions

In this paper, we describe active cannula design, modeling, and experiments, providing an archival unification of technical results previously published in conference proceedings [15], [18], as well as broadening the background and discussion. We explore the hypothesis that overall cannula shape locally minimizes stored elastic energy and examine the significance of modeling torsional effects in addition to bending effects. The energy model enables analytical prediction of a bifurcation in the energy landscape as a function of actuator positions, which matches experimental observations and provides a means for calibration. Additionally, the model predicts feature and tip positions of our prototype active cannula, providing another independent calibration method. We experimentally show close agreement of the two calibration methods and validate that fitted parameter values lie near expected ranges derived from tube physical characteristics.

Using the energy model, we present a framework for computing the forward kinematics of multilink active cannulas via energy minimization. Experimental results validate the kinematic framework and demonstrate that modeling torsional effects is essential to predict active cannula bifurcation behavior and physical shape.

II. Cannula Design and Mechanics

The active cannula shown in Fig. 1 is made of three precurved elastic tubes, with a largest section diameter of 2.4 mm, tapering to a smallest section diameter of 0.8 mm.[1] While prototype active cannulas discussed in this paper are all made from Nitinol[2] (e.g., Fig. 1), we note that active cannulas may be made of a variety of elastic materials, including plastics. Desirable characteristics are materials that can sustain high strain without damage, and have high torsional rigidity compared to their flexural rigidity. Nitinol is one such material and has been reported to sustain recoverable strains of as much as $\varepsilon = 11\%$ [28], although most estimates are approximately 8%.

Forward kinematics for an active cannula is a description of complete device shape in terms of joint variables, namely component tube linear positions and rotations. This requires a model of how precurved tubes cause one another to bend. To simplify analysis, we consider circular precurvature; however, other variable curvature shapes may be suited to specific applications or surgical interventions and may even be customized individually to achieve specific goals. The modeling process provides various design insights, including curvature limits to prevent plastic deformation of cannula component tubes. The one "link" model developed shortly maps the axial rotation angles of concentric curved tubes to their common equilibrium curvature and bending plane.

A. Modeling Assumptions

The main (experimentally validated) assumptions in the model presented next are that tubes can be considered to

[1]Note that active cannulas can be made significantly smaller in diameter than this first prototype by reducing individual tube diameters and the tolerances between tubes.

[2]While the active cannula prototypes described in this paper exploit Nitinol's superelastic properties only, we note that appropriate heat transmission mechanisms could also be included to activate shape memory effects.

directly apply moments to one another, and that (due to circular component tube precurvatures) those moments can be considered constant along the length of a link. Other modeling assumptions include linear elasticity (constant Young's modulus) and the dominance of bending effects over the shear effects induced by bending.[3] Finally, we assume that all torsional compliance is lumped into the long, straight transmission.

B. Active Cannula Features

Features of the active cannula design that seem particularly appealing are that miniaturization *enhances* dexterity (smaller tube diameters permit larger precurvatures, as discussed in Section II-D) and that compliance is tunable through design (adjusting individual tube stiffnesses by choosing wall thickness, diameters, preformed shapes, or material properties) as well as configuration. Compliance (whether intentionally tuned or not) is inherent in the design and is expected to enhance active cannula safety, reducing potential tissue damage in the event of inadvertent cannula/tissue contact.

It is often convenient to model snake-like robots as a mathematical curve (e.g., a series of circular arcs [30] or more general curves). Robot kinematics is approximated, more or less accurately depending on the robot and the configuration, as the curve. However, with the active cannula's circular precurvatures, and provided model assumptions drawn from experimental observation in this paper and in [14] and [15] are accurate, no approximation is needed. The active cannula will actually be a series of circular arcs. Further, when representing many other continuum robot designs as a mathematical curve, it can be quite challenging to fully describe the effect of physical joint limits, and the robot may inadvertently damage itself [31]. An appropriately designed active cannula (Section II-D and II-E) is not subject to this danger since it combines both elastic elements and force transmission elements directly into the extensible backbone. Active cannulas have no joint limits and can be designed to preclude self-damage everywhere in their configuration spaces. Any joint limits that are present are an artifact of a specific actuation unit design, and actuation units can, in principle, be constructed to allow as much motion as desired.

C. Precurvature Limits

The selection of the initial curvature to be preset into each tube is an important design consideration. Without specific clinical requirements, smaller radii of precurvature are generally desirable since they enable the cannula to negotiate tighter turns within anatomy. However, if the radii of precurvature are chosen too small, the cannula may damage itself (plastically deforming one or more of its component tubes) at certain positions in its configuration space.

While some medical interventions may not require access to the full configuration space (for example, one or more tubes may not be required to perform 360° rotations) and, thus, permit smaller radii of curvature, it is generally desirable to design tube precurvatures to eliminate the possibility of active cannula self-damage. This can be accomplished by ensuring that the maximum strain in all component tubes is maintained within the elastic region for all possible robot configurations.

Material recoverable strain is expected to be the primary consideration in choosing active cannula precurvatures, rendering Nitinol, with its large recoverable strain, a good material from which to make active cannula tubes. The relationship between material strain limits and maximum precurvature for a single tube, such that it can fully straighten without plastic deformation, is

$$\kappa = \frac{2\varepsilon}{D(1+\varepsilon)} \tag{1}$$

where ε is the strain and D is the tube outer diameter, as derived in [15] and [19]. Note that the curvature of the tube is inversely proportional to D. Thus, smaller tubes can sustain higher preset curvatures. This means that as the design is miniaturized, it will be able to reach around tighter corners, enhancing its dexterity. Tradeoffs for enhancing dexterity in this manner may be a reduction in stiffness or size of the central working channel.

Other design considerations may necessitate choosing a curvature somewhat less than this maximum value. For example, finite torsional stiffness means that there may be a bifurcation in the energy landscape as described in Sections III–IV; this bifurcation leads to a "snapping" of the active cannula, and it may be desirable to avoid this either by design of tube precurvatures or by restricting the joint angles to bifurcation-free ranges.

Another possible design criteria for curvatures is to choose them to preclude cannula self-damage. Generally, one or more tubes in the active cannula will have to bend back upon itself (further than straight) to "negative curvature." To evaluate the design implications of this (Section II-E), we must first examine the effect of precurved coplanar tubes on one another.

D. In-Plane Beam Mechanics

If several precurved tubes are placed concentrically, their curvatures will "interfere" with one another, causing bending and making the combined shape different from the natural rest shapes of individual tubes. It is this interference effect, combined with both rotation and extension–retraction of the tubes, that we use to change the shape of the active cannula. To describe the complete shape of the active cannula, we must first develop a model for the shape of a single "link" composed of several overlapping concentric curved tubes. Each link will be a circular arc with an associated curvature and plane.

Fig. 2 shows the effect of concentric tubes of different precurvatures on one another in the planar case. Here, the tubes have not been axially rotated with respect to one another and their natural curvature planes are aligned. The Bernoulli–Euler beam equation describes the instantaneous curvature of an initially straight beam with respect to arc length as

$$\kappa = \frac{d\phi}{ds} = \frac{M}{EI} \tag{2}$$

where ϕ is the angle measured from the tangent vector, s is the arc length, M is the moment applied to a differential element,

[3]This is a common assumption for thin beams [29, ch. 8] and permits the use of (2) to relate tangent angle to bending moment.

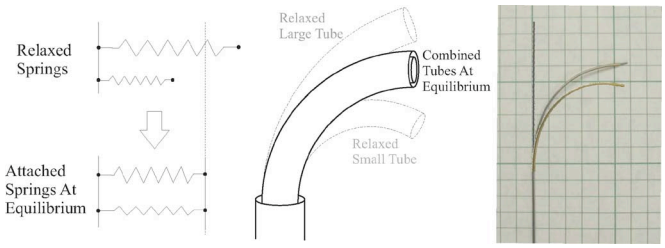

Fig. 2. (Left) Parallel spring position equilibrium. (Middle) Analogous curved tube equilibrium. Dashed lines indicate natural tube curvatures, solid lines show the effect of placing tubes inside one another. (Right) Photograph of experiment. Initially straight wire and initially curved tube shapes are superimposed on a photograph of the combined wire and tube.

E is the modulus of elasticity (Young's modulus), and I is the cross-sectional moment of inertia.

Using circular preset tube curvatures permits an idealization of the beam equation. Because the curvature is constant for each tube, the tube will apply a constant moment on the tubes exterior to or within it, namely

$$M = EI\,\Delta\kappa. \tag{3}$$

If the tubes are axially aligned so that they naturally curve in the same plane, (3) is analogous to Hooke's law for a linear spring, i.e., "$F = K\,\Delta X$," as illustrated in Fig. 2. In the analogy, the bending stiffness EI of a tube corresponds to the spring constant, the moment M corresponds to the linear force, and curvature κ is a "position" variable. Just as we can describe the equilibrium position of linear springs of different lengths and stiffnesses when connected in parallel by a force balance, we can describe the resultant curvature of two overlapping tubes whose natural planes of curvature are aligned by

$$\kappa = \frac{E_1 I_1 k_1 + E_2 I_2 k_2}{E_1 I_1 + E_2 I_2} \qquad \text{or} \qquad \kappa = \frac{\sum_{i=1}^{n} E_i I_i k_i}{\sum_{i=1}^{n} E_i I_i} \tag{4}$$

for n tubes, where k_i's are the preformed curvatures of the individual tubes. This model is verified experimentally in Section II-F.

E. Design Implications of Tube Interaction

Rotating one tube 180° with respect to the other is analogous to attaching a linear spring to the other side of the wall, so that its initial position is now $-x$ ($-k$ for the tube). Thus, the equilibrium position of the more compliant of the two springs will, in general, be on the opposite side of zero from where it begins. For the tubes, this corresponds to bending further than straight (further than zero curvature). We can define $\Delta\kappa_{\max,i}$ for tube i as $\Delta\kappa_{\max,i} = k_i - \kappa$ when all other tubes are rotated 180° with respect to the tube in question. The $\Delta\kappa_{\max}$ values for each tube must be kept at or below the bound in (1), to prevent the possibility of plastic deformation in any tube for all possible active cannula configurations.

F. In-Plane Experimental Validation

We experimentally validated the in-plane beam mechanics model (4) using curved Nitinol tubes and straight wires, as shown in Fig. 2. Table I illustrates our results. The Nitinol tubes were plastically deformed to an initial curvature k_1. The wires were initially straight, with $k_2 = 0$. Photographs of each tube were taken against a 5-mm grid both before and after wires were inserted. The best-fit circle was then determined manually by examining the photographs and adjusting the diameter of a fitting circle until it closely matched the curvature in the photograph. We estimated that the error associated with fitting a circle in this way was within 10% of the actual circle radius. It would be preferable to have Nitinol preshaped by the manufacturer in the desired circular shape, but this would have added significant cost at the very small quantities used in this study. It is also possible to heat set a curvature into straight Nitinol tubes after purchase, but this is a delicate process. Nitinol requires a specific heat-time profile that is strongly dependent on small changes in composition of the alloy to set a shape while retaining superelasticity. However, we do expect heat-shaping to be the most desirable long-term method of creating precurvature in Nitinol tubes.

TABLE I
VERIFICATION OF BERNOULLI–EULER BASED BEAM MECHANICS MODEL

Tube			Wire		Combined	
ID (mm)	OD (mm)	k_1 (1/mm)	OD (mm)	k_2 (1/mm)	r meas (mm)	r pred (mm)
0.622	0.800	0.044	0.430	0	26.0	25.5
0.965	1.27	0.020	0.800	0	62.5	61.2
1.47	1.78	0.021	1.30	0	75.5	72.8
2.01	2.39	0.028	1.60	0	49.8	50.5

G. Axial Tube Rotation

When curved tubes are rotated axially, their natural planes of curvature are no longer aligned and the direction of the bending moments they apply changes. In addition to bending moments, a torsional moment is also generated by such motion. We will begin in this section by considering bending only and proceed to incorporate torsion into the model in Section II-H.

1) Intuition: If two precurved tubes with same stiffness (EI) and initial curvature k are placed within one another and rotated 90° with respect to one another, one would expect the plane of the combined tubes to be directly between their natural planes, at 45°. One would also expect them to straighten out somewhat since at 180° they would be completely straight. This is illustrated in Fig. 3. If the tubes do not have the same stiffness, then the combined plane should shift toward the stiffer tube.

2) Beam Mechanics Model With Rotation: Intuition can be formalized in terms of the beam mechanics described earlier. Tubes whose natural planes are rotated with respect to one another exert a moment on one another about their respective x-axes, which is caused by their initial precurvature about this direction. Fig. 3 shows a cross-sectional view of the tubes inside one another. The tubes are rotated by angles θ_i, and the equilibrium plane angle is ϕ.

As before, each tube applies $M = EI(\Delta\kappa)$, but now this moment has two component projections on the base frame x and y axes. Assuming torsional rigidity, the component projections are the same for the x- and y-axes of any copy of the base frame

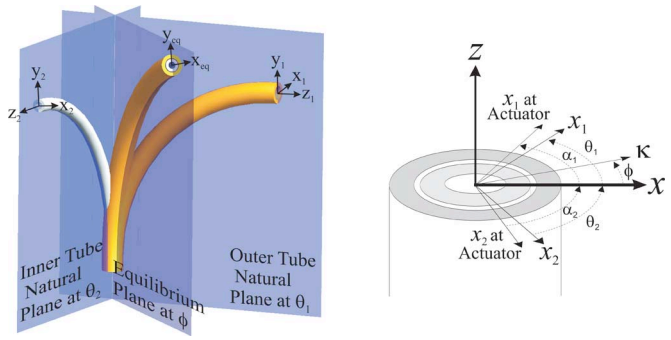

Fig. 3. (Left) If two concentric curved tubes are axially rotated with respect to one another, they will reach a minimum energy equilibrium between their individual or "natural" planes. They will also begin to straighten from the curvature they would exhibit with aligned natural planes. (Right) Cross-sectional view of tubes at link base. We assume that the curved sections are torsionally rigid, so this is also the cross section along the entire link. When transmissional torsion is included, actuator inputs α_i's are not, in general, equivalent to link base angles Θ_i for each tube.

slid along the link in the z-direction. Summing the moments about x and y yields

$$\chi = \frac{\sum_i E_i I_i k_i \cos\theta_i}{\sum_i E_i I_i} \quad \text{and} \quad \gamma = \frac{\sum_i E_i I_i k_i \sin\theta_i}{\sum_i E_i I_i} \tag{5}$$

respectively.

Assuming infinite torsional rigidity, (5) would be sufficient to describe the shape of a complete active cannula made up of several such links (as described in Section III). However, since these are superelastic tubes, torsional deformation will occur. It will be particularly important in the straight transmission sections of the tubes that lie between the actuators and the first curved link, since these transmissions are long relative to the curved sections.

H. Flexural and Torsional Elastic Energy

If transmissional torsion between actuators and the first curved link is included in the model, link-base tube angles (θ_i) will no longer be the same as actuator input angles (α_i). The cross section of the tubes will then be as shown in Fig. 3 (right).

To determine link base angles, we will use a minimum energy strategy (Section III-B). Doing so requires expressing the total energy of the cannula using both bending and torsional terms. The elastic energy of a beam of length ℓ in pure bending is

$$U_{\text{bend}} = \int_0^{\ell} \frac{M(s)^2}{2EI} ds. \tag{6}$$

When the moment is constant along the length of the beam, this reduces to

$$U_{\text{bend}} = \frac{EI\ell}{2} \Delta\kappa^2. \tag{7}$$

Torsional energy for a beam is given by

$$U_{\text{tors}} = \int_0^{L} \frac{\tau(s)^2}{2GJ} ds \tag{8}$$

where τ is torque applied, G is the shear modulus, and J is the polar moment of inertia. When torque is constant along the length of the beam (as it is for the straight transmission sections), and the angle between ends of the beam is $\alpha - \theta$, this reduces to

$$U_{\text{tors}} = \frac{GJ}{2L}(\alpha - \theta)^2. \tag{9}$$

In contrast to bending moments, torsional moments generated by tube interaction will not be constant along the curved links, as they are in the straight transmissions. These energy relationships facilitate the energy method used for kinematics in the next section.

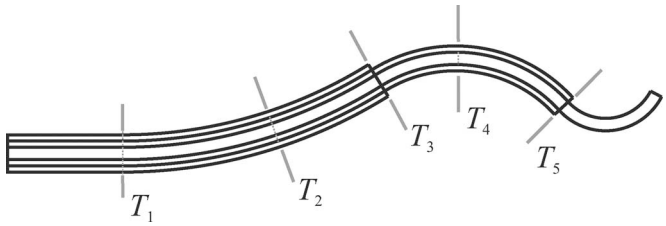

Fig. 4. "Links" or regions of unique overlap of a three–tube cannula composed of tubes like those in the upper image of Fig. 5. Links start and end at transition points, and the jth link is between T_j and T_{j+1}. In this configuration, the largest tube transitions from straight to the left of T_1 to curved to the right. The same is true of the middle tube at T_2 and the smallest tube at T_4.

III. Kinematics via Minimum Energy

The kinematics of continuum and hyperredundant robots are often decomposed into two mappings. One is from actuator (joint) space to arc parameters (curvature, plane, and length of each section), while the other is from arc parameters to Cartesian positions of the robot. We follow a similar strategy in the analysis of the active cannula. The first mapping (Section III-A and III-B) is generally robot-specific since the type of actuators and design of the robot strongly influence how actuators affect arc parameters. The mapping from arc parameters to shape (Section III-C), on the other hand, is common to all robots that can be modeled as piecewise constant curvature.

The shape of an active cannula is defined by a sequence of unique overlap regions ("links") between transition points T_j, as shown in Fig. 4. Each of these links remains circular both by assumption and observation [14], [15], although the bending plane and curvature change as tubes are axially rotated. Thus, an active cannula is piecewise-constant curvature, consisting of a series of constant curvature links, where each is tangent to adjacent links.

A. Determining Link Lengths

The first step in describing the shape of an active cannula is determining the number of links and link lengths. These are defined by component tube transition point locations, which are functions of tube preshaped geometry (Fig. 5) and translational "joint" positions of tube bases. These combine to create a sequence of links between transition points as shown in Fig. 4. For the three–tube active cannula illustrated (where each tube has a straight transmission followed by a single circular arc), there are five curved links. More generally, n tubes result in $2n - 1$ links

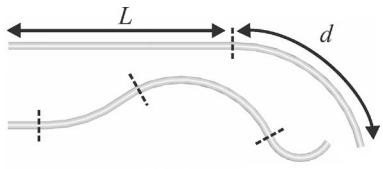

Fig. 5. (Top) Tubes used in all active cannula studies to date (including this paper) consist of a straight transmission of length L, with a constant curvature section of length d at one end. (Bottom) Our models presented here are, in principle, general enough to account for piecewise circular/straight tubes with multiple transition points.

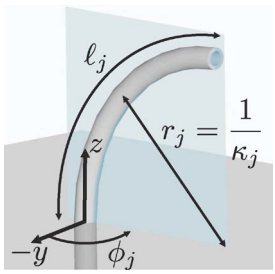

Fig. 6. Arc parameters of a curved link consist of curvature (κ_j), equilibrium plane angle (ϕ_j), and arc length (ℓ_j), as shown.

(or $2n$, if an initial straight link is included). The length of some links reaches zero when transition points align. It is straightforward to determine the lengths of the links in the cannula, given actuator displacements and component tube geometries.

For the example in Fig. 4, the lengths of the m (in this case five) regions of overlap $\ell_j, j \in \{1, \ldots, m\}$ are given by the actuator translational positions of the n tubes $\rho_i, i \in \{1, \ldots, n\}$, and the lengths of the curved portion d_i of each tube are given as

$$\begin{aligned}
\ell_1 &= \rho_2 - \rho_1 \\
\ell_2 &= \rho_1 + d_1 - \rho_2 \\
\ell_3 &= \rho_3 - \rho_1 - d_1 \\
\ell_4 &= \rho_2 + d_2 - \rho_3 \\
\ell_5 &= \rho_3 + d_3 - \rho_2 - d_2. \qquad (10)
\end{aligned}$$

A general procedure that is easily amenable to software implementation for determining all ℓ_j is to sort transition points in terms of arc length, with link lengths given by differences between adjacent transition points. We also note that if component tubes themselves have more than one transition point, additional active cannula links result.

B. From Joint Space to Arc Parameters

Active cannula joint space is parametrized by axial translations $\boldsymbol{\rho}$ and rotations $\boldsymbol{\alpha}$ applied at the base of each tube, namely $\boldsymbol{q} = (\alpha_1, \rho_1, \ldots, \alpha_n, \rho_n)$. In what follows, the subscript $i \in \{1, \ldots, n\}$ refers to tube number, while $j \in \{1, \ldots, m\}$ refers to link number. Cannula links are circular segments described by the arc parameters curvature, plane, and arc length $(\kappa_j, \phi_j, \ell_j)$, as shown in Fig. 6. The mapping from $\boldsymbol{q}$ to $\boldsymbol{\ell}$ was described in the previous section, while the mapping from $\boldsymbol{q}$ to $(\boldsymbol{\kappa}, \phi)$ can be accomplished by generalizing the single-link model described previously, as follows.

Attach a coordinate frame T_j at the base of the link by sliding a copy of the cannula base frame along the backbone (without rotation about z) to the base of the link. The model then yields x and y curvature components for the link in the link frame as

$$\chi_j = \frac{\sum_i E_i I_i k_{i,j} \cos\theta_{i,j}}{\sum_i E_i I_i} \quad \text{and} \quad \gamma_j = \frac{\sum_i E_i I_i k_{i,j} \sin\theta_{i,j}}{\sum_i E_i I_i}$$

respectively. The sums over $i \in \Lambda_j$ only include the tubes that overlap the jth link. Since the intrinsic (preformed) curvature is piecewise constant along each tube, $k_{i,j}$ denotes the intrinsic curvature of the ith tube in the jth link. Note that these values change as a function of the actuator translations because the overlapping regions change as described before, i.e., $k_{i,j}$ is a function of $\boldsymbol{\rho}$. E_i is the elastic modulus, I_i is the cross-sectional moment of inertia, and $\theta_{i,j}$ is the axial ith tube angle about the jth link frame z-axis. There is a direct relationship between curvature components and arc parameters, namely

$$\phi_j = \tan^{-1}\left(\frac{\gamma_j}{\chi_j}\right) \qquad \text{and} \qquad \kappa_j = \sqrt{\chi_j^2 + \gamma_j^2}. \qquad (11)$$

Neglecting torsional compliance completely (i.e., assuming infinite torsional rigidity), $\theta_{i,j} = \theta_{i,0} \equiv \alpha_i$ for all j, which results in a direct symbolic mapping (11) from actuator space to arc parameters for each link. However, when transmissional torsion is included, $\theta_{i,1}$ no longer equals actuator input α_i because the straight transmission will "wind up" as torque is applied at the actuators. Since transmissions are generally long compared to curved sections, we assume that tubes can be modeled as infinitely torsionally stiff beyond T_1, implying that $\theta_{i,j} = \theta_{i,1} \equiv \psi_i$ for all $j > 1$. With these definitions, applying (7) and (9) in all directions for all tubes yields the key modeling result of this paper, an expression for the total elastic energy stored in the system

$$\begin{aligned}
U(\psi_1, \ldots, \psi_n) = &\underbrace{\sum_{i=1}^{n} \frac{G_i J_i}{2L_i}(\alpha_i - \psi_i)^2}_{\text{transmission torsion}} \\
&+ \underbrace{\sum_{j=1}^{m} \sum_{i \in \Lambda_j} \frac{E_i I_i \ell_j}{2}(\chi_j - k_{i,j}\cos(\psi_i))^2}_{x\text{-direction bending}} \\
&+ \underbrace{\sum_{j=1}^{m} \sum_{i \in \Lambda_j} \frac{E_i I_i \ell_j}{2}(\gamma_j - k_{i,j}\sin(\psi_i))^2}_{y\text{-direction bending}} \qquad (12)
\end{aligned}$$

where G is the shear modulus, J is the polar moment of inertia, L is the length of straight transmission between actuator and curved section of tube, and, as mentioned previously, $i \in \Lambda_j$ are the tubes that are present in the jth link.

We assume that actuator inputs influence the system quasi-statically in the sense that as we move the actuators, the system remains at a local minimum energy. Thus, the angles at the end of the straight transmission $(\psi_1, \ldots, \psi_n)$ are always assumed to be at a local minimum of (12).

The forward kinematics is calculated by finding local minima of (12). As we describe in Section IV, there can be multiple such minima, and the particular minimum of (12) in which the robot finds itself depends on the path traversed through joint space to reach current joint angles.

C. End-Effector Pose

The shape of the cannula is defined by the arc parameters and the product of exponentials formula. The joint twists associated with arc parameters are

$$\xi_\phi = [\, v_\phi^T \quad \omega_\phi^T \,] = [\, 0 \quad 0 \quad 0 \quad 0 \quad 0 \quad 1 \,]^T$$
$$\xi_j(\boldsymbol{q}) = [\, v_j^T \quad \omega_j^T \,] = [\, 0 \quad 0 \quad 1 \quad \kappa_j(\boldsymbol{q}) \quad 0 \quad 0 \,]^T \quad (13)$$

where v and ω are linear and angular differential motions. Thus, ξ_ϕ corresponds to rotation of a link and ξ_j corresponds to translation along a link. Then, as described in [32, ch. 2], the full kinematics of the mechanism can be described by the product of exponentials formula

$$g(\boldsymbol{q}) = \prod_{j=1}^{m} e^{\left(\widehat{\xi_\phi}(\Delta\phi_j(q))\right)} e^{\left(\widehat{\xi_j(q)}\ell_j(q)\right)} \quad (14)$$

where $\Delta\phi_j = \phi_j - \phi_{j-1}$ and $g \in \mathrm{SE}(3)$ is the transformation from cannula base to tip. Thus, each cannula link contributes a pair of exponentials to the overall kinematics, and the pairs are written left to right in order of increasing link number.

IV. Three–Link Case

For the remainder of this paper, we consider the specific case of three links (two tubes), which corresponds to the prototype with which we perform experimental validation and parameter fitting in Section V-C and D. For $n = 2$, we have $m = 2n - 1 = 3$ regions of overlap, only the middle of which contains two curved tubes. In this case, the energy (12) is

$$U(\psi_1, \psi_2) = \frac{c_1}{2}(\alpha_1 - \psi_1)^2 + \frac{c_2}{2}(\alpha_2 - \psi_2)^2 + \ell_2 c_3 \left(\frac{k_1}{2k_2} - \cos(\psi_1 - \psi_2) + \frac{k_2}{2k_1} \right) + \frac{\ell_1}{2} c_4 k_1^2 \quad (15)$$

where $c_1 = G_1 J_1 / L_1, c_2 = G_2 J_2 / L_2, c_3 = (E_1 I_1 E_2 I_2 k_1 k_2)/(E_1 I_1 + E_2 I_2)$, and $c_4 = (E_1 I_1 E_2 I_2)/(E_1 I_1 + E_2 I_2)$. To find the critical points of U, we set the gradient with respect to ψ to zero

$$\nabla U = \begin{bmatrix} -c_1(\alpha_1 - \psi_1) + \ell_2 c_3 \, \sin(\psi_1 - \psi_2) \\ -c_2(\alpha_2 - \psi_2) - \ell_2 c_3 \, \sin(\psi_1 - \psi_2) \end{bmatrix} = 0 \quad (16)$$

where the unknowns are (ψ_2, ψ_1) and (α_1, α_2) are the inputs, which can be simplified to

$$\psi_1 - \alpha_1 = \ell_2 b_1 \, \sin(\alpha_2 + b_2 \alpha_1 - (1 + b_2)\psi_1) \quad (17)$$

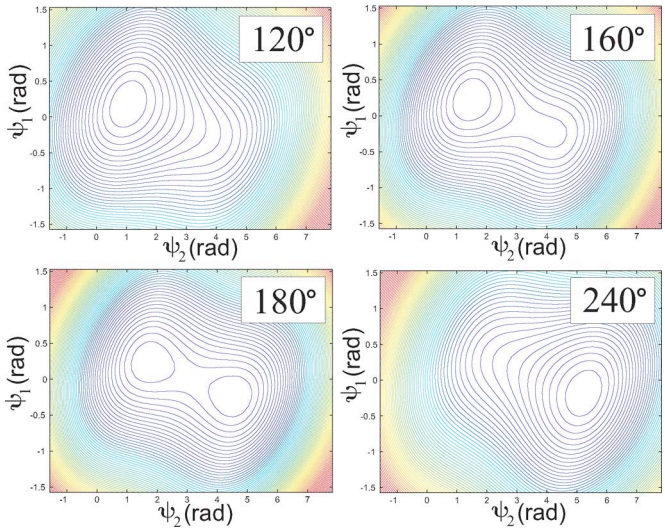

Fig. 7. Contour plots of the energy landscape as the angular difference between the tube bases is increased. Angular difference between the base inputs of the two tubes is listed in the upper right corner of each plot. For small angular differences, there is only one global minimum. As the angular difference approaches 180°, two appear. Beyond 180°, the new minimum becomes the global minimum, and eventually the only minimum. These plots are for the "partial overlap" experiment in Section V and are made using nominal parameter values.

where

$$b_1 = \frac{c_3}{c_1} \quad \text{and} \quad b_2 = \frac{c_1}{c_2}. \quad (18)$$

The transcendental equation (17) has the same form as the well-known Kepler equation from celestial mechanics [33]. In our experimental results (Section V), we use a fifth-order Taylor expansion of the sine term about the most recent available previous value of ψ_1. We note that, in practice, on a robotic system, a close approximation for the true value of ψ_1 about which to expand is readily available, because generally the robot will only move a small amount between computer servo cycles. We choose the real root of the resulting polynomial that is closest to the previous value as the solution. While this procedure worked well for our data set (there always appeared to be one, and only one, noncomplex root), a more careful solution of (16) that is guaranteed to find all possible critical points as well as resolve the path-dependence issue is a topic left to future study.

A. Bifurcation and "Snapping"

For small actuator angle differences $(\alpha_2 - \alpha_1)$, there is a unique global minimum of the (12) with respect to ψ. As the difference between actuator input angles approaches 180°, a bifurcation in the energy landscape in the torsion angles (ψ_1, ψ_2) introduces two spurious critical points: a saddle and local minimum (see Fig. 7). As the actuator input difference approaches 180° from below, the new minimum deepens, and the minimum in which the system rests rises, until at $(\alpha_2 - \alpha_1) = 180°$, the heights of the minima are equal. Just beyond an actuator difference of 180°, the spurious minimum actually becomes the global minimum, but the system remains in the original local minimum due to the "torsional windup" history effect. As the

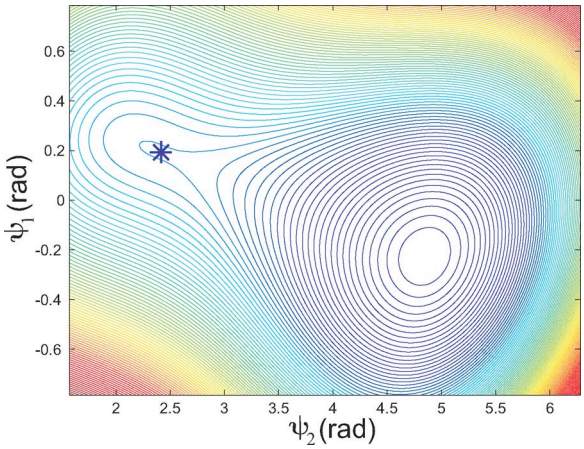

Fig. 8. Contour plot of the energy function at the bifurcation point. The * denotes the position of the system [from (20) and (21)] just before the energy landscape bifurcates, and the cannula "snaps" to a new minimum.

input angle difference continues to increase, the system remains in the local minimum until it reaches another bifurcation, at which point, the local minimum disappears, leaving only the global minimum above 180°. At this point, the system "snaps" to the global minimum, releasing built-up torsional energy.

There are at least three reasons that this bifurcation effect is important to study and model. First, in surgery and other practical applications it is likely to be undesirable (and potentially dangerous) for the cannula to rapidly and forcefully move to a new location, so it is important to be able to predict when bifurcation will occur. Second, as will be described in Section V, bifurcation provides a calibration method independent of position sensing. Third, bifurcation is a structural prediction of the model that can be verified experimentally in the laboratory.

At a bifurcation point, the local minimum and saddle merge. This effect happens when the Hessian is singular (concavity changes) while simultaneously the gradient is zero (critical point). This is illustrated in Fig. 8. The Hessian is singular when

$$\det\left(\frac{\partial^2 U}{\partial \psi^2}\right) = c_1 c_2 + (c_1 + c_2)\ell_2 c_3 \cos(\psi_1 - \psi_2) = 0. \tag{19}$$

Combining this with the zero gradient constraint (16), it is possible (for a fixed α_1) to solve for the ψ_1, ψ_2, and input α_2 at which the bifurcation occurs. Without loss of generality, assuming $\alpha_1 = 0$, these are given by

$$\psi_1 = \frac{1}{c_1}\sqrt{(\ell_2 c_3)^2 - \left(\frac{c_1 c_2}{c_1 + c_2}\right)^2} \tag{20}$$

$$\psi_2 = \psi_1 + \cos^{-1}\left(-\frac{c_1 c_2}{\ell_2 c_3 (c_1 + c_2)}\right) \tag{21}$$

$$\alpha_2 = \sqrt{(\ell_2 \beta)^2 + \cos^{-1}\left(\frac{1}{\ell_2 \beta}\right)} \tag{22}$$

where the bifurcation parameter $\beta = -c_3/c_2 - c_3/c_1$. In Section V-C, we experimentally determine input angles that cause bifurcation and use the closed-form expression of (22) to facilitate bifurcation parameter fitting.

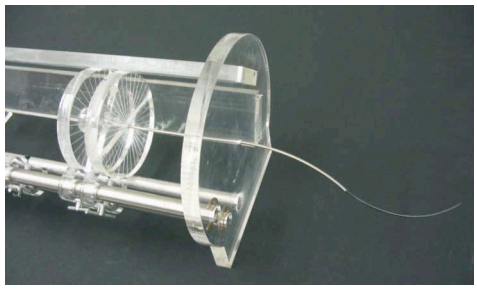

Fig. 9. Manual actuation mechanism. Both tube and wire have input circular handles etched to encode rotation and the support structure features a linear ruler etched to encode translation. Spring pin locking mechanisms hold the wheels at desired linear and angular positions.

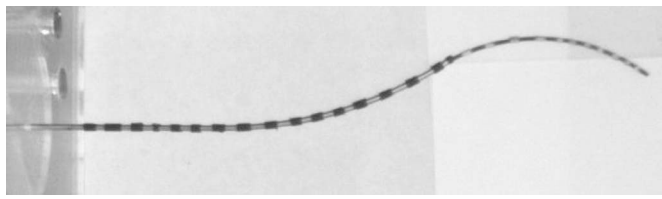

Fig. 10. Experimental photograph from one of the stereo cameras showing the cannula with fiducial markers.

V. Experiments and Parameter Fitting

Two types of experiments were undertaken to evaluate the ability of the model discussed in Sections III and IV to capture cannula shape, bifurcation behavior, and endpoint position. A second goal of these experiments was to calibrate the active cannula, estimating model parameters.

A. Materials and Sensing

We used a simple manual actuation mechanism to examine the theoretical predictions developed in previous sections. The device provides acrylic disc handles affixed to tube bases as shown in Fig. 9. Radial lines etched on the discs every 10° enable manual axial rotation to desired angles. The linear translations of the discs can be set using a 1-mm resolution ruler etched onto the acrylic support structure. Spring-loaded locking pins can fix wheel positions in both degrees of freedom.

Acrylic handles were affixed to the base of a 2.39-mm-outside-diameter (OD) and 2.01-mm-inside-diameter (ID) Nitinol tube, and 1.60-mm-diameter Nitinol wire. The tube has a 93.5 mm straight transmission and a 92.3 mm curved section created via plastic deformation with a curvature of 0.0099/mm. The wire has a 218.5 mm straight transmission and an 85-mm-long circular curved section created via plastic deformation with a curvature of 0.0138/mm. The specific tube dimensions used in this experiment were selected to enable a workspace wherein the cannula is easily viewable by off-the-shelf optical cameras.

Fiducial markers (bands of black tape) were placed along the cannula for stereo triangulation, as shown in Fig. 10. The positions of these fiducials were sensed using a stereo vision

system composed of two calibrated XCD-X710 (Sony, Inc.) firewire cameras running at a resolution of 1024×768 pixels. One source of error in this data collection procedure is the accuracy of manual point selection in images, which is estimated at 2 pixels or 0.6 mm. Another is fiducial size (they are not perfect points), causing small differences in intended selection locations. We estimate fiducial dimensions to introduce error of no more than the diameter of the wire itself (1.6 mm). Thus, our overall vision system measurement error is estimated at approximately 2.2 mm.

B. Parameter Estimates From Physical Quantities

Writing model parameters in terms of basic material properties and measured dimensions is the first step in determining reasonable physical expectations of parameter values. This can be accomplished by combining (18) with the formula for cross-sectional inertia of a circular section ($I = (\pi/64)(\mathrm{OD}^4 - \mathrm{ID}^4)$), and the relationships between shear and bending quantities ($J = 2I$ and $E = 2G(1+\nu)$, where ν is Poisson's ratio), to produce

$$b_1 = \frac{E_2 I_2 L_1 k_1 k_2 (1+\nu_1)}{E_1 I_1 + E_2 I_2}, \qquad b_2 = \frac{E_1 I_1 L_2 (1+\nu_2)}{E_2 I_2 L_1 (1+\nu_1)}. \tag{23}$$

Expected parameter ranges for b_1 and b_2 can be deduced from the uncertainty in each quantity upon which they depend. Nitinol dimensions are specified by the manufacturer (Nitinol Devices and Components, Inc.) to ± 0.0010 in, while the elastic modulus E is reported as 41–75 MPa. Poisson's ratio is not quoted, but is often taken to be approximately 0.35 for Nitinol. It has also been noted that plastic deformation can increase Poisson's ratio for Nitinol to 0.5 or more [34], so we will assume a range of 0.30–0.55. Measurement errors in straight transmission lengths are estimated to be 1 mm, and measurement accuracy of curvature was estimated at 10% (Section II-F). Applying error propagation, the variance in parameters b can be determined by[4]

$$\Omega_b = J_{b\varsigma}\ \Omega_\varsigma\ J_{b\varsigma}^T \tag{24}$$

where Ω_ς is a diagonal matrix of variances in each quantity upon which $\boldsymbol{b}$ depends (denoted by the ς) and $J_{b\varsigma}$ is the Jacobian between parameters and quantities containing error ($J_{b\varsigma} = \partial \boldsymbol{b}/\partial \varsigma$). The square roots of the diagonal entries of Ω_b yield the variance in parameter values, based on the uncertainty in the physical quantities upon which they depend. These yield a b_1 range of 3.36–7.06 and a b_2 range of 3.14–8.45. A similar calculation for the bifurcation parameter ($\beta = -b_1(b_2+1)$) yields a range for β of -41.45 to -29.41. These ranges provide a basis for comparison with fitted parameter values produced by the calibration procedures described shortly.

C. Bifurcation Point Experiment

To experimentally determine the bifurcation parameter β for the cannula, the tube was fixed in place, and the wire was rotated until the bifurcation angle was reached, at which time, the cannula visibly "snapped" to the new global minimum. This was done for 12 linear translational positions in 5 mm increments for ℓ_2 from 82.3 to 27.3 mm. A sampling of this data is shown in Table II. Note that the input angle at which bifurcation occurs is always more than 180° and is often significantly more. This illustrates the torsional windup that occurs in active cannulas, even with the relatively short transmission of our prototype. The β-parameter was fit to this data using Matlab's `nlinfit`, which computes a nonlinear regression using least squares. Using this procedure, we estimated β at -44.91, with a 95% confidence interval of ± 2.02, which is near (though slightly below) the range described in Section V-B. In Section V-D, we explain how unmodeled effects should be expected to increase the magnitude of the experimental β in this type of experiment, but we first determine β again in Section V-D through a different procedure that uses data more uniformly distributed over cannula workspace.

TABLE II
SAMPLE EXPERIMENTAL BIFURCATION ANGLES FOR VARIOUS LENGTHS OF CURVED TUBE/WIRE OVERLAP

ℓ_2 (mm)	82.3	72.3	62.3	52.3	42.3	32.3	27.3
α_2 (deg)	295	283	265	240	225	205	200

An important feature of active cannula bifurcation behavior is that it ceases to occur for some values of β. For a given cannula with fixed curvatures, this corresponds to a minimum length of curved tube overlap. Below this length, the energy landscape always has a single global minimum, and thus, it is not possible to simultaneously satisfy (16) and (19). Using $\beta = -44.91$, the predicted ℓ_2 from (22) is 22.3 mm (the value at which $\cos^{-1}(1/\ell_2\beta)$ becomes undefined). Minima at slightly larger ℓ_2 values will be very near one another (and very near 180°), and friction will also mask very small bifurcation motions. These effects cause a first discernible experimental cannula bifurcation at $\ell_2 = 27.3$ mm, which is only slightly higher than the value predicted above.

It is also possible to view the point at which bifurcation ceases as a design tool. Cannula curvatures can be selected so that bifurcation is prevented even for complete overlap. For fixed curvatures, we will further explore ℓ_2 prediction in comparison to calibrated parameter values using shape data.

D. Shape Experiment

Using the stereo camera system described before and with the base of the tube fixed, cannula shape information was captured for multiple input angles at two distinct linear positions of the base of the wire. One, called the "full overlap" position, caused $\ell_1 = 10$ mm (tube curved, wire straight), $\ell_2 = 82.3$ mm (both curved), and $\ell_3 = 2.7$ mm (tube ended, only curved wire present). The other, called the "partial overlap" position, caused $\ell_1 = 48.0$ mm, $\ell_2 = 44.3$ mm, and $\ell_3 = 40.7$ mm, with the same tube and wire combinations in each link. For the full overlap case, 15-input angles were applied at 20° increments from 0° to 280°. For the partial overlap case, 11 input angles were applied at 20° increments from 0° to 200°.

[4]For the sake of estimating parameter variances, we assume that physical parameter ranges are equally scaled variances.

Using data collected from these experiments, we fit b_1 and b_2. The transformation between the stereo camera coordinate frame and a frame fixed at the base of the cannula was first estimated using point cloud registration [35]. Images of a 15-mm checkerboard pattern (with corners at known physical locations with respect to the cannula base frame) were captured. Sixteen corners on the checkerboard were triangulated with the stereo vision system. Since the points were coplanar, this registration was only expected to provide a rough estimate of the frame transformation. Thus, six "nuisance parameters" (a 3-vector for position and a 3-vector for orientation with magnitude of rotation encoded as length) describing the cannula base frame were included in the calibration procedure and initialized with the results from the point cloud registration.

Before fitting parameters, we experimentally investigated our expectation that cannula tip positions are both repeatable and symmetric with respect to input angle. We collected additional tip position data for negative α_2 values from zero to -180° for partial overlap, and zero to -240° for full overlap, in 60° increments. Reflecting tip positions about the *y*–*z* plane for comparison to positive α_2 inputs of the same magnitudes, we found an average tip position difference of only 2.39 mm. Considering sensitivity to frame transformation error, these results appear to be within our measurement uncertainty.

Parameter fitting was accomplished using Matlab's `fmincon`, with angular nuisance parameter bounds set to ± 0.349,[5] from initial estimates. The objective function was the sum of Euclidean distances from experimental to theoretical tip positions (14), outer tube endpoints (14) (up to link $m-1$), and positions of fiducial bands nearest the cannula base (a fixed distance along the straight cannula transmission between T_0 and T_1). The optimization rapidly converged to $b_1 = 7.92$ and $b_2 = 4.11$ from a wide range of initial b_1 and b_2 values. Nuisance parameters showed only small changes during optimization, with cannula base frame orientation moving 4.4° while position of the base tape fiducial translated 1.1 mm. These small changes in nuisance parameters are reasonable given the coplanar data used to compute our initial frame transformation estimate. Average tip error was reduced from 10.1 mm (22.10 mm maximum) with no fitting to 3.0 mm (8.76 mm maximum) with fitting. Given estimated measurement error of 1 mm in individual tube straight and curved lengths, and the 2.2 mm estimated sensing error, average tip error of 3 mm appears reasonable.

Furthermore, the fitted b_2 was within the range determined in Section V-B, while b_1 was near it. The energy bifurcation parameter they imply ($\beta = -40.49$) is also now within its estimated parameter range. Small differences in β compared to the bifurcation experiment (which produced $\beta = -44.91$) are the results one would expect from unmodeled torsional deformation (in the curved regions) and unmodeled friction. Both would serve to increase the magnitude of the bifurcation experiment estimate of β. In that experiment, all data were from regions in joint space where the highest possible cannula internal forces occur. This contrasts the shape experiment, which used data more uniformly distributed over the joint space. If effects of friction and unmodeled torsion cause a 5.4% reduction in each experimental bifurcation angle (see Table II), this would account for the difference in β. Further, $\beta = -40.49$ generates the prediction that bifurcation will cease at $\ell_2 = 24.7$ mm, only 2.6 mm less than the experimental value ($\ell_2 = 27.3$ mm found in Section V-C), and somewhat closer than $\ell_2 = 22.3$ mm from the bifurcation experiment.

[5]This is equivalent of $\pm 20^\circ$ converted to radians. However, since magnitude is also encoded in these variables, this bound cannot be strictly thought of as an angle.

E. Importance of Torsion

As we have described in this paper, including torsion in active cannula models leads to transcendental equations. Because of this (as outlined in Section I-A), models have been proposed in the literature that assume infinite torsional rigidity and treat active cannula kinematics as a pure beam bending problem. While this is analytically attractive, our experimental results indicate that assuming infinite torsional rigidity precludes accurate prediction of active cannula shape. Without torsion, there is only one model parameter present in the kinematic model (11), namely the ratio of tube flexural rigidities ($B = E_1 I_1 / E_2 I_2$). The feasible range for B using the tolerances described in Section V-B is 0.630–4.33.

Applying the same fitting procedures described in Section V-D to the torsionless case, we first obtained a prefitting tip error of 24.78 mm (54.32 mm maximum). We then fit model and frame nuisance parameters and found convergence over a wide range of initial values to $B = 3.98$, nuisance angle $= 36.93^\circ$, and nuisance distance $= 1.11$ mm. Average tip error was reduced to 13.60 mm (31.48 mm maximum). Thus, tip errors remain large for the torsionless model even with calibration. Further, the angular nuisance parameters changed significantly during optimization, resulting in highly inaccurate predictions of overall cannula shape throughout the workspace.

To explore the possibility that nuisance parameters were not well suited for torsionless calibration, we also applied calibration procedures to the torsionless model while holding the nuisance parameters fixed at values known to give approximately correct frame transformations. Fixing nuisance parameters at the initial frame estimate from the point cloud registration, we optimized B alone and determined a value of 3.59. This resulted in average tip error of 23.50 mm (53.94 mm maximum). The other approximately correct set of nuisance parameters available are the calibrated values found for the torsion-included model in Section V-D. Holding nuisance parameters fixed at these values, we determined $B = 3.98$. This resulted in an average tip error of 22.20 mm (52.39 mm maximum).

Thus, all efforts to calibrate torsionless active cannula models result in large tip errors. This indicates that active cannula models that do not include torsion are structurally insufficient for making accurate predictions of our experimental active cannula shape. They also cannot predict bifurcation behavior since infinite torsional rigidity implies that tube angles are equal to base input angles at all points along the cannula. Results are illustrated visually in Fig. 11 for a parameter value in the middle of the physically expected range and using the initial frame

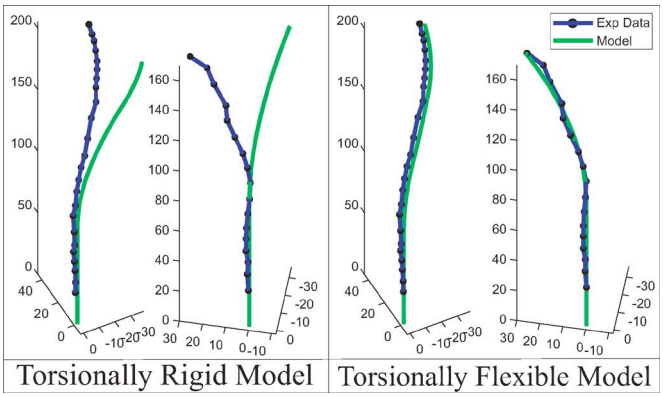

Fig. 11. Experimental data and model predictions of the partial and full overlap conditions at the final input angles before bifurcation (200° and 280°, respectively). Note that these are also the input angles with the greatest overall tip error for each case. These results show that torsion is a vital part of an accurate active cannula kinematic model.

estimate. If the cannula design was modified to use a different material with higher torsional rigidity for straight transmissions, the torsionless model may be more successful. However, doing so would be challenging from a prototype manufacturing standpoint. For our current all-Nitinol prototype, inability to account for torsional windup in the torsionless model makes it inaccurate, except in a small neighborhood of $(\alpha_2 - \alpha_1) = 0$.

VI. Discussion

We envision applying the basic framework presented in this paper to a diverse family of both robotic and manual surgical devices, each customized to different application requirements. These may be specified in a variety of ways, including desired workspaces, forces, or end-effectors. The design and modeling results presented in this paper will facilitate future efforts to customize active cannulas for each new application, as described in [19, Sec. 4.8].

Some future applications of active cannulas will require coordinated motion of all degrees of freedom simultaneously. This is facilitated by a robotic actuation unit, and one design for such a device can be found in [19, Sec. 4.2]. In many applications, it will be important to match the workspace of the cannula to application requirements, and the forward kinematic results provided in this paper can be used to describe active cannula workspace, given component tube geometries. The inverse question of synthesizing individual geometries from a required workspace volume is an open question for future research. Similarly while inverse kinematics has been studied under the assumption of infinite torsional rigidity [20], future work will be necessary to generalize inverse kinematics to include torsional effects and possibly other unmodeled effects.

Examples of such unmodeled effects include torsion in curved sections, frictional effects, and the implications of the modeling assumptions made in Section II-A. All such effects likely contribute to the small differences (average 3 mm) between model predictions and experimental results. Of these effects, the authors hypothesize that unmodeled torsion in the curved sections is the most significant. This is based primarily on qualitative observation of the prototype cannula used in this paper, which does not exhibit significant hysteresis or stick-slip behavior, even without lubrication. However, it is possible that with active cannulas of different designs (e.g., smaller diameters or intratube tolerances), frictional effects may become more pronounced and active cannula models may require enhancements to account for it.

The model described in this paper without further enhancements is likely to be accurate enough for some medical tasks. An example is thermal ablation in the liver, which does not require high accuracy. In higher accuracy applications, model-based controllers may also be applied that are robust to modeling errors [36]. Similarly, in teleoperated tasks, the human operator can compensate for modeling errors. Cardiac access (the motivation for the catheter-based industrial robots mentioned earlier [8]) is one medical procedure where continuum robots can be operated under teleoperateive control. Medical applications requiring greater accuracy (e.g., microsurgery on the retina) will require future modeling enhancements.

VII. Conclusion

This paper provides design, modeling, analysis, and experimental results that are foundational steps toward realizing the potential of active cannulas in medicine and other applications. Analysis relating tube elastic deformation limits to precurvatures and tools to characterize and (if desired) prevent bifurcation behavior are among the design contributions presented. Beam-mechanics-based models of cannula link shape were derived and generalized into a framework for forward kinematics of multilink cannulas. This framework is closed form in the torsionless case, and it was shown how torsion can be included through energy minimization. The importance of torsion and the accuracy of the model were evaluated experimentally and parameters were fit through two complementary calibration procedures that agree well with expected parameter ranges calculated from material property tolerances and physical geometry. Experimental results lead to the conclusion that when modeling active cannulas, torsion must be taken into account to describe cannula shape well and to make models structurally capable of predicting observed bifurcation behavior.

This poses some interesting future challenges. One is to solve various robotics problems for active cannulas (e.g., motion planning and inverse kinematics) in an analytically more complex setting without the aid of closed-form kinematics. Another is to approach the problem from a design perspective and explore tube materials that will increase torsional stiffness while maintaining bending flexibility.

Acknowledgment

The authors would like to thank A. Okamura for contributing to our first conference paper on this subject and R. Taylor for his significant insight into active cannula design and application.

REFERENCES

[1] I. D. Walker, D. Dawson, T. Flash, F. Grasso, R. Hanlon, B. Hochner, W. M. Kier, C. Pagano, C. Rahn, and Q. Zhang, "Continuum robot arms inspired by cephalopods," in *Proc. SPIE Conf. Unmanned Ground Vehicles*, Orlando, FL, Mar. 2005, pp. 303–314.

[2] V. Anderson and R. Horn, "Tensor arm manipulator design," *ASME Trans.*, vol. 67-DE-57, no. 2, pp. 1–12, 1967.

[3] S. Hirose, *Biologically Inspired Robots, Snake-Like Locomotors and Manipulators*. London, U.K.: Oxford Univ. Press, 1993.

[4] G. S. Chirikjian, "Kinematic synthesis of mechanisms and robotic manipulators with binary actuators," *J. Mech. Design*, vol. 117, pp. 573–580, 1995.

[5] M. W. Hannan and I. D. Walker, "Kinematics and the implementation of an elephant's trunk manipulator and other continuum style robots," *J. Robot. Syst.*, vol. 20, no. 2, pp. 45–63, 2003.

[6] B. A. Jones and I. D. Walker, "Practical kinematics for real-time implementation of continuum robots," *IEEE Trans. Robot.*, vol. 22, no. 6, pp. 1087–1099, Dec. 2006.

[7] P. Dario, M. C. Carrozza, M. Marcacci, S. D'Attanasio, B. Magnami, and G. M. O. Tonet, "A novel mechatronic tool for computer-assisted arthroscopy," *IEEE Trans. Inf. Technol. Biomed.*, vol. 4, no. 1, pp. 15–29, Mar. 2000.

[8] (2008, Oct. 25) [Online]. Available: http://www.hansenmedical.com/

[9] N. Simaan, R. Taylor, and P. Flint, "A dexterous system for laryngeal surgery," in *Proc. IEEE Int. Conf. Robot. Autom.*, 2004, pp. 351–357.

[10] L. Adhami and E. Coste-Maniere, "Optimal planning for minimally invasive surgical robots," *Trans. Robot. Autom.*, vol. 19, no. 5, pp. 854–863, 2003.

[11] J. W. Cannon, J. A. Stoll, S. D. Sehla, P. E. Dupont, R. D. Howe, and D. F. Torchina, "Port placement planning in robot-assisted coronary artery bypass," *IEEE Trans. Robot. Autom.*, vol. 19, no. 5, pp. 912–917, Oct. 2003.

[12] J. Furusho, T. Katsuragi, T. Kikuchi, T. Suzuki, H. Tanaka, Y. Chiba, and H. Horio, "Curved multi-tube systems for fetal blood sampling and treatments of organs like brain and breast," *J. Comput. Assist. Radiol. Surg.*, vol. 1, pp. 223–226, 2006.

[13] M. Loser, "A new robotic system for visually controlled percutaneous interventions under X-ray or CT-fluoroscopy," M.S. thesis, Albert-Ludwig-Univ.. Freiburg, Germany, Sep. 2002.

[14] P. Sears and P. E. Dupont, "A steerable needle technology using curved concentric tubes," in *Proc. IEEE/RSJ Int. Conf. Intell. Robots Syst.*, Oct. 9–15, 2006, pp. 2850–2856.

[15] R. J. Webster, III, A. M. Okamura, and N. J. Cowan, "Toward active cannulas: Miniature snake-like surgical robots," in *Proc. IEEE/RSJ Int. Conf. Intell. Robots Syst.* Oct. 9–15, 2006, pp. 2857–2863.

[16] H. M. Hegazy, R. L. Carrau, C. H. Snyderman, A. Kassam, and J. Zweig, "Transnasal endoscopic repair of cerebrospinal fluid rhinorrhea: A meta-analysis," *Laryngoscope*, vol. 110, pp. 1166–1172, 2000.

[17] A. B. Kassam, C. Snyderman, P. Gardner, R. Carrau, and R. Spiro, "The expanded endonasal approach: A fully endoscopic transnasal approach and resection of the odontoid process: Technical case report," *Operative Neurosurg.*, vol. 57, pp. 213–214, 2005.

[18] R. J. Webster, III, A. M. Okamura, and N. J. Cowan, "Kinematics and calibration of active cannulas," in *Proc. IEEE Int. Conf. Robot. Autom.*, 2008, pp. 3888–3895.

[19] R. J. Webster, III, "Design and mechanics of continuum robots for surgery," Ph.D. dissertation, Mech. Eng., Johns Hopkins Univ., Baltimore, MD, Dec. 2007.

[20] P. Sears and P. E. Dupont, "Inverse kinematics of concentric tube steerable needles," in *Proc. IEEE Int. Conf. Robot. Autom.*, 2007, pp. 1887–1892.

[21] M. Terayama, J. Furusho, and M. Monden, "Curved multi-tube device for path-error correction in a needle-insertion system," *Int. J. Med. Robot. Comput. Assist. Surg.*, vol. 3, no. 2, pp. 125–134, 2007.

[22] S. Okazawa, R. Ebrahimi, J. Chuang, S. E. Salcudean, and R. Rohling, "Hand-held steerable needle device," *IEEE/ASME Trans. Mechatron.*, vol. 10, no. 3, pp. 285–296, Jun. 2005.

[23] W. Daum, "A deflectable needle assembly," Patent 6 572 593, 2003.

[24] D. Glozman and M. Shoham, "Image-guided robotic flexible needle steering," *IEEE Trans. Robot.*, vol. 23, no. 3, pp. 459–467, Jun. 2007.

[25] V. Kallem and N. J. Cowan, "Image guidance of flexible bevel-tip needles," *IEEE Trans. Robot.*, to be published.

[26] R. J. Webster, III, J. S. Kim, N. J. Cowan, G. S. Chirikjian, and A. M. Okamura, "Nonholonomic modeling of needle steering," *Int. J. Robot. Res.*, vol. 25, no. 5/6, pp. 509–526, May/Jun. 2006.

[27] S. P. DiMaio and S. E. Salcudean, "Needle insertion modeling and simulation," *IEEE Trans. Robot. Autom.*, vol. 19, no. 5, pp. 864–875, Oct. 2003.

[28] T. W. Duerig, A. R. Pelton, and D. Stockel, "Superelastic nitinol for medical devices," *Med. Plastics Biomaterials Mag.*, vol. 4, pp. 30–43, Mar. 1997.

[29] S. H. Crandall, N. C. Dahl, and T. J. Lardner, *An Introduction to the Mechanics of Solids*. New York: McGraw-Hill, 2007 (ISBN: 0070667349).

[30] B. A. Jones and I. D. Walker, "Kinematics for multisection continuum robots," *IEEE Trans. Robot.*, vol. 22, no. 1, pp. 43–55, Feb. 2006.

[31] B. A. Jones, W. McMahan, and I. D. Walker, "Practical kinematics for real-time implimentation of continuum robots," in *Proc. IEEE Int. Conf. Robot. Autom.*, 2006, pp. 1840–1847.

[32] R. M. Murray, Z. Li, and S. S. Sastry, *A Mathematical Introduction to Robotic Manipulation*. Boca Raton, FL: CRC, 1994.

[33] H. Goldstein, *Classical Mechanics*, 2nd ed. Reading, MA: Addison-Wesley, 1980, pp. 101–102; 123–124.

[34] P. M. White, "Stress induced interposed connector," Patent 6 257 593, 2001.

[35] K. S. Arun, T. S. Huang, and S. D. Blostein, "Least-squares fitting of two 3-D point sets," *IEEE Trans. Pattern Anal. Mach. Intell.*, vol. PAMI-9, no. 5, pp. 698–700, Sep. 1987.

[36] R. J. Webster, III, J. P. Swenson, J. M. Romano, and N. J. Cowan, "Closed-form differential kinematics for concentric-tube continuum robots with application to visual servoing," in *Proc. 11th Int. Symp. Exp. Robot. Springer Tracts Adv. Robot.*, to be published.

Robert J. Webster, III (S'97–M'08) received the B.S. degree in electrical engineering from Clemson University, Clemson, SC, in 2002 and the M.S. and Ph.D. degrees in mechanical engineering from the Johns Hopkins University, Baltimore, MD, in 2004 and 2007, respectively.

In 2008, he joined the faculty of Vanderbilt University, Nashville, TN as an Assistant Professor of mechanical engineering and is currently the Director of the Medical and Electromechanical Design (MED) Laboratory. His current research interests include medical robotics, image-guided surgery, human–machine interfaces, and continuum robotics.

Joseph M. Romano (S'07) received the B.S. degree in computer science and engineering mechanics from Johns Hopkins University, Baltimore, MD, in 2007. He is currently working toward the Ph.D. degree in mechanical engineering with the University of Pennsylvania, Philadelphia.

He was an Undergraduate Researcher with the National Science Foundation (NSF) Engineering Research Center for Computer-Integrated Surgical Systems and Technology. His current research interests include human–machine interaction, mechatronic design, and vision-based control for robotic systems.

Noah J. Cowan (S'98–M'01) received the B.S. degree in electrical engineering from Ohio State University, Columbus, in 1995 and the M.S. and Ph.D. degrees in electrical engineering and computer science from the University of Michigan, Ann Arbor, in 1997 and 2001, respectively.

From 2001 to 2003, he was a Postdoctoral Fellow in both integrative biology and computer science at the University of California, Berkeley. In 2003, he became an Assistant Professor of mechanical engineering with the Faculty of Johns Hopkins University, Baltimore, MD, where he is currently the Director of the Locomotion in Mechanical and Biological Systems (LIMBS) Laboratory. His current research interests include multisensory control of locomotion in robotics and biology, bioinspired robotics, and vision-based control with application to medical robotics.

Prof. Cowan was the recipient of the William H. Huggins Award for excellence in teaching in 2004. He is also the recipient of a Rackham Doctoral Fellowship from the University of Michigan.